

Plasmonic Terahertz Nonlinearity in Graphene Disks

Jeong Woo Han, Matthew L. Chin, Sebastian Matschy, Jayaprakash Poojali, Angelika Seidl, Stephan Winnerl, Hassan A. Hafez, Dmitry Turchinovich, Gagan Kumar, Rachael L. Myers-Ward, Matthew T. Dejarld, Kevin M. Daniels, Howard Dennis Drew, Thomas E. Murphy, and Martin Mittendorff*

The discovery of graphene and its unique optical and electronic properties has triggered intense developments in a vast number of optoelectronic applications, especially in spectral regions that are not easily accessible with conventional semiconductors. Particularly in the THz regime, where the free-carrier interaction with low-energetic photons usually dominates, detectors and modulators based on graphene often feature an improved response time. Nevertheless, the light–matter interaction suffers from the small interaction volume. One way to enhance the efficiency of such devices at elevated frequencies is by patterning graphene into plasmonic structures like disks. In addition to the increased linear absorption, the plasmon resonance also creates a strong, surface-localized field that enhances the nonlinear optical response. While experimental studies so far have focused on hot carrier effects, theoretical studies also suggest an increase in the nonlinearity beyond thermal effects. Herein, polarization-dependent pump-probe measurements on graphene disks that disentangle the contributions of thermal and plasmonic nonlinearity are presented. An increase in the pump-induced transmission is observed when pump and probe radiation are copolarized. To further elucidate the interplay of thermal and plasmonic effects, a model that supports the origin of the polarization-dependent enhancement of the observed THz nonlinearities is developed.

1. Introduction

The exploitation of plasmonically enhanced absorption in graphene elements^[1–8] has been demonstrated to be a powerful method to improve THz devices like detectors,^[9,10] emitters,^[11–13] or modulators.^[14–17] In particular, all optical modulators are enabled by optical nonlinearities,^[18–20] which are often considered at high photon energy, that is, for interband transitions.^[21] In this case, multiple effects are usually considered to contribute to the optical nonlinearity, for example, Pauli blocking or Kerr nonlinearity.^[22–28] Pauli blocking is caused by the optically excited carriers that fill up the final state and thus decrease the absorption. The Kerr effect is a third-order nonlinear process that is linked to the optical conductivity being dependent on the driving electric field.^[29] While Pauli blocking only occurs at high photon energy and/or low Fermi energy, the Kerr nonlinearity can also be observed for intraband processes that are relevant for the low photon

J. W. Han, S. Matschy, M. Mittendorff
Fakultät für Physik
Universität Duisburg-Essen
47057 Duisburg, Germany
E-mail: martin.mittendorff@uni-due.de

M. L. Chin, J. Poojali, T. E. Murphy
Institute for Research in Electronics and Applied Physics
University of Maryland
College Park, MD 20740, USA

K. M. Daniels
Department of Electrical and Computer Engineering
University of Maryland
College Park, MD 20740, USA

H. D. Drew
Center for Nanophysics and Advanced Materials
University of Maryland
College Park, MD 20740, USA


M. L. Chin
U.S. Army Research Laboratory
Adelphi, MD 20783, USA

A. Seidl, S. Winnerl
Institut für Ionenstrahlphysik und Materialforschung
Helmholtz-Zentrum Dresden-Rossendorf
01328 Dresden, Germany

H. A. Hafez, D. Turchinovich
Fakultät für Physik
Universität Bielefeld
33615 Bielefeld, Germany

G. Kumar
Department of Physics, Guwahati
Indian Institute of Technology Guwahati
Guwahati, Assam 781039, India

R. L. Myers-Ward, M. T. Dejarld
U.S. Naval Research Laboratory
Washington, DC 20375, USA

 The ORCID identification number(s) for the author(s) of this article can be found under <https://doi.org/10.1002/adpr.202100218>.

© 2021 The Authors. Advanced Photonics Research published by Wiley-VCH GmbH. This is an open access article under the terms of the Creative Commons Attribution License, which permits use, distribution and reproduction in any medium, provided the original work is properly cited.

DOI: 10.1002/adpr.202100218

energy in the THz regime. In addition, hot carrier effects contribute to the nonlinear THz response, even enabling efficient high harmonic generation.^[30] During a THz field cycle, the carriers are heated efficiently by Drude absorption, leading to a decrease in conductivity. Thus, the current is not proportional to the electric field, but is significantly distorted, which leads to the strong harmonic generation. A similar THz nonlinearity can be observed in plasmonic graphene elements: patterning graphene into micrometer-sized ribbons can increase the extinction to above 30% at resonance.^[31] When those graphene elements are excited by intense and short THz pulses, carrier heating leads to a change in transmission by about 10%.^[32]

This THz nonlinearity was analyzed by a two-temperature model, indicating that hot carriers dominate the observed effects.^[32,33] While this thermal effect is in agreement with recent theoretical studies, additional contributions to the nonlinear absorption are expected. As for the interband processes, Kerr nonlinearities are predicted to play an important role for the nonlinear properties in graphene THz plasmons. Here, we present an experimental study that disentangles thermal effects from Kerr nonlinearities via polarization-resolved pump-probe measurements. The experimental results are well reproduced by a two-temperature model that also includes Kerr nonlinearities, that is, the conductivity of graphene depends on the strength of the driving electric field.

2. Results and Discussions

To detect the Kerr nonlinearity experimentally, we perform narrow-band THz pump-probe experiments on a square array of graphene disks in transmission geometry. The disks offer an isotropic plasmonic response, so the linear absorption is independent of the THz polarization. A sketch of the plasmonic array of graphene disks is shown in **Figure 1a**. The graphene disks were fabricated via oxygen plasma etching of quasi-freestanding bilayer graphene on SiC. Details on the fabrication method can be found in various studies.^[32,34] The radius R and periodicity Λ of the graphene disks are 1.48 and 1.85 μm , respectively. Note that we use the same sample as in the study by Chin et al.^[34] The dimensions R and Λ determine the plasmon frequency of 3.5 THz, which was confirmed via time-domain THz spectroscopy of the graphene disks.^[34] The circular geometry of the plasmonic elements in a square array enables the investigation of the origin of the Kerr nonlinearity via polarization-dependent pump-probe measurements: when pump and probe radiation are copolarized, thermal effects and Kerr nonlinearity contribute to the pump-probe signal. For cross-polarized radiation, that is, the polarization of the pump and probe pulses are perpendicular to each other, the thermal effects contribute as much as for the copolarized case, while the Kerr nonlinearity is expected to be significantly reduced. The plasmonic nonlinearity is polarization sensitive as the charge carrier motion in perpendicular directions is partially decoupled (for details, see Supporting Information [SI]). Thus, we can measure the nonthermal contributions to the THz nonlinearity by subtracting the curve of the cross-polarized measurements from the copolarized case. To quantitatively analyze the underlying physics behind the nonlinearity, we develop the simulation considering thermal and

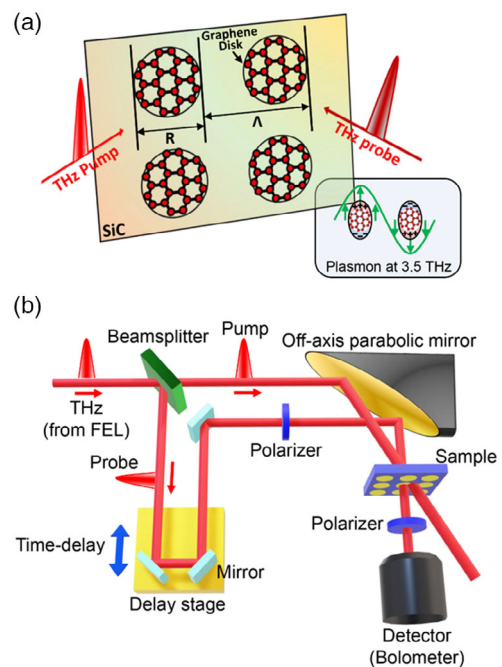


Figure 1. Sketch of graphene disks and experimental setup. a) Illustration of graphene disks and plasmon. Resonance frequency of plasmon is 3.5 THz. R (1.48 μm) and Λ (1.85 μm) are the radii and the period of graphene disks. b) Schematic diagram of the experimental setup for THz pump and probe measurement.

Kerr nonlinearities, which exhibits good agreement with the experimental data.

To investigate the THz nonlinear response of the graphene disks, the pump-induced change in transmission is measured as a function of the time delay between the pump pulse and probe pulse (cf. Figure 1b). The THz pulses are generated by a free-electron laser (FEL) (FELBE facility at Helmholtz-Zentrum Dresden-Rossendorf), which provides a constant pulse train of narrow-band THz pulses with a repetition rate of 13 MHz. The center wavelength of THz pulses was tuned to the plasmon frequency of 3.5 THz to efficiently activate the resonant excitation of the plasmons. A pellicle beam sampler is used to split off about 1% of the radiation that is subsequently delayed by a mechanical stage. Off-axis parabolic mirrors are utilized to focus the pump and probe THz beams onto the graphene disks and collect the transmitted probe radiation. The sample is kept inside an optical cryostat at a temperature θ_L of 10 K. For the measurements with linearly polarized radiation, a wire-grid polarizer is introduced in the probe beam at an angle of 45° with respect to the pump radiation. A second polarizer behind the sample is used to pick the co- or crosspolarized component. As the linear polarization can induce an anisotropic carrier distribution in momentum space, potentially leading to a polarization dependence of the pump-probe signal,^[35] we perform additional measurements using circularly polarized light by introducing quarter-wave plates in the pump and probe beams. In this case, anisotropic heat distribution is excluded.

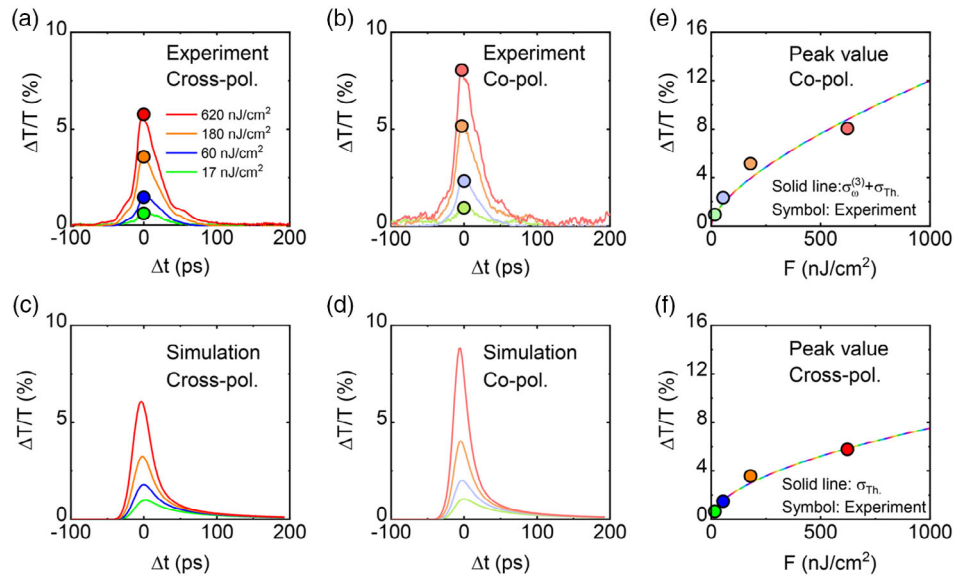


Figure 2. Change of THz transmission probed with linearly polarized radiation. Experimentally measured change of transmission $\Delta T/T$ at 3.5 THz with the a) cross- and b) copolarization configurations. Input fluences are changed from 620 to 17 nJ cm⁻². Circles denote the peak values of the transmission. c) Simulated $\Delta T/T$ corresponding to (a). Only thermal nonlinearity σ_{Th} is considered. d) Simulated $\Delta T/T$ corresponding to (b). σ_{Th} and Kerr nonlinearity $\sigma_{\omega}^{(3)}$ are considered. e,f) Peak values of $\Delta T/T$ with the fluence-dependence for co- and crosspolarizations, respectively. Circles shown in (e) and (f) are taken from (b) and (a), respectively. Lines denote simulation results.

Figure 2a,b shows the experimental data taken with linearly polarized radiation in cross- and copolarized configurations, respectively. $\Delta T/T$ indicates the relative change in transmission caused by the pump pulse. In both cases, an increased transmission that scales sublinearly to the pump fluence is observed. After the peak change in transmission is reached, the signal decays within several tens of picoseconds, as was observed in earlier studies on graphene ribbons.^[32,33] A stronger change in transmission is observed in the copolarized geometry compared with the cross-polarized case, which is expected, as both thermal and Kerr nonlinearities should lead to a decrease in absorption. The peak changes in transmission, denoted by circles in Figure 2a,b, are plotted as a function of the pump fluence in Figure 2e,f, respectively. Thermal nonlinearities are expected to lead to a polarization-independent change in the probe transmission as the optically excited hot carriers rapidly equilibrate in momentum space, achieving a thermal distribution of carriers that affects both polarizations identically. For the case of the copolarized geometry, in addition to the thermal effects, the THz probe beam directly interacts with plasmons that are driven by the pump beam. To exclude spurious differences that could be caused by cryostat windows or anisotropic disks, we experimentally confirm that the pump-probe signals show the same response whether or not we rotate all polarizations involved by 90° (see SI).

To analyze the origin of different responses on $\Delta T/T$ depending on the configurations of polarizations, we perform numerical simulations of the transient changes in optical properties. The model uses a 2D sheet conductivity, incorporating both a two-temperature hot-carrier response and Kerr nonlinearity. The sheet optical conductivity $\sigma_{\omega}^{(1)}$, which depends on the electronic

temperature θ , provides the linear response of the plasmons based on a Drude-like model. In combination with the filling factor of $\eta \approx 0.6$, which takes into account the fraction of the area that is covered by the graphene disks, the optical sheet conductivity can be calculated by^[33,36]

$$\sigma_{\omega}^{(1)} = \eta \frac{iD(\theta)}{\pi} \frac{1}{(\omega_{\text{eff}}(\theta) + i\Gamma(\theta))} \quad (1)$$

where $\omega_{\text{eff}}(\theta) = (\omega^2 - \omega_{p0}^2(\theta))/\omega$ with ω and ω_{p0} being the photon frequency and the plasmon frequency (3.5 THz), respectively. The subscript on the optical sheet conductivity, ω , indicates that the conductivity is evaluated at the frequency of the incident THz beam. As the FEL is tuned to excite the plasmons resonantly, the effective frequency is $\omega_{\text{eff}}(\theta) = 0$ when the system is in equilibrium. The superscript of (1) in Equation (1) denotes the linear response to the electric field, that is, $j_{\omega}^{(1)}(\omega) = \sigma_{\omega}^{(1)}(\omega)E$, where j and E are the electrical current density and the electric field, respectively. Even though this expression is by itself linear, the temporal evolution of the electron temperature leads to the characteristic variation of the optical properties. One of the main causes of strong dependence of the optical properties on the electron temperature is the density of states, which increases linearly with energy. As the Fermi edge is smeared out in case of the hot carriers, the chemical potential has to decrease to keep the number of electrons constant. A decrease in the chemical potential leads, in turn, to a decrease in the Drude weight and a red-shift of the plasmon resonance. The fractional decrease in Drude weight is proportional to the square of the electron temperature.^[32] Furthermore, the scattering rate is increased as the electron temperature is increased.^[32] The pump-induced temporal evolution of the electron temperature

can be determined by solving the balance equation, and a temperature-dependent cooling rate for supercollision cooling is considered phenomenologically (see Supporting Information).

As the disk pattern of our sample is centrosymmetric, even-order nonlinear processes are excluded. To obtain the nonlinear response beyond thermal effects, we consider the Kerr effect, which is a third-order process. By applying the same methodology as in Equation (1), the Kerr conductivity^[37] at plasmon resonance $\sigma_{\omega}^{(3)}(\omega)$ can be expressed as

$$\sigma_{\omega}^{(3)} = \eta \frac{i9e^6 v_F^2}{4\pi \hbar^4 D(\theta)} \times \frac{1}{(\omega_{\text{eff}}(\theta) + i\Gamma(\theta))(-\omega_{\text{eff}}(\theta) + i\Gamma(\theta))(2\omega_{\text{eff}}(\theta) + i\Gamma(\theta))} \quad (2)$$

where \hbar is the reduced Planck's constant and $v_F = 10^6 \text{ m s}^{-1}$ is the Fermi velocity for charge carriers in graphene.^[38,39] The probe current density can be written as $J_2 = \sigma^{(1)} E_2 + \frac{1}{2} \sigma^{(3)} [(E_1^* \cdot E_1) E_2 + (E_1 \cdot E_2) E_1^* + (E_1^* \cdot E_2) E_1]$, where the subscript 1 (2) represents the pump (probe) field. Thus, the conductivity can be written as $\sigma_{\text{tot}} = \sigma_{\omega}^{(1)} + \sigma_{\omega}^{(3)} [E \cdot E]$, where the first term represents the linear conductivity and the second term represents the Kerr nonlinearity. The electric field of the pump pulse E is included for copolarized radiation and set to zero for cross-polarized cases. The θ evolutions for various pump fluences resulting from the interplay of thermal and plasmonic effects are provided as a function of the delay time in **Figure 3a**. Based on the pump power, pulse duration, and the focus size, the electric field evolution is calculated, as shown in the inset of **Figure 3b**.

For a quantitative comparison of the simulation results with the experimental data, we calculate the transmission through the sample with an equivalent circuit model. The light–matter interaction (absorption, reflection, and transmission) can be fully described by the complex conductivity at the interface between substrate and vacuum. Details on the model are described by Jadidi et al.^[33] With this model, the transmission can be written as

$$T = \frac{4\sqrt{\epsilon_1 \epsilon_2}}{Z_0^2 \left| \frac{\sqrt{\epsilon_1 + \sqrt{\epsilon_2}}}{z_0} + \sigma_{\text{tot}} \right|^2} \quad (3)$$

where Z_0 is the impedance of free space being 377Ω . ϵ_1 and ϵ_2 are dielectric constants for vacuum and the SiC substrate, which are 1 and 12.5, respectively. Simulation results for the co- and crosspolarized configurations are shown in **Figure 2c,d**, respectively. The model resembles the pump fluence dependence of the experimental results qualitatively and quantitatively well, as clearly shown in **Figure 2e** (copolarization) and **f** (crosspolarization).

As mentioned earlier, a second set of pump-probe data was taken with circularly polarized pump and probe radiation to avoid spurious signals caused by anisotropic carrier distribution. **Figure 4a,b** shows the experimental data for the counter- and copolarized geometries, respectively. As for the case of linear polarization, a sublinear increase in the pump-probe signal with increasing pump fluence is observed (see **Figure 4e,f**). Again, this trend can be well reproduced by our simulation, illustrated in **Figure 4c,d**, for counter- and copolarized configurations, respectively. For the simulation, we again consider the electric field of the pump pulse to calculate the Kerr nonlinearity for the copolarized case, and $E = 0$ for the counterpolarized radiation. To extract the Kerr contribution of the pump-probe signals, the $\Delta T/T$ of the counterpolarized measurements was subtracted from the data of copolarized case in **Figure 4g,h**, respectively, at a pump fluence of 80 nJ cm^{-2} . As can be seen in experiment and simulation, the duration of the plasmonic nonlinearity is determined by the pulse duration of the FEL. This is consistent with the expectation that the Kerr nonlinearity manifests only in the presence of the pump field. Furthermore, this reflects the short plasmon lifetime, which is about 10% of the FEL pulse duration, as can be concluded from linear spectroscopy.^[34] Even at room temperature, a clear pump-probe signal can be observed (see **Figure 4i**). As expected from measurements on unpatterned graphene,^[20] at higher temperatures, the peak change in transmission is decreased significantly and the carrier relaxation is decreased to or below the temporal resolution of the experiment. Remarkably, the thermal and Kerr contributions can still be distinguished. This is of great importance for potential applications of graphene plasmonic nonlinear elements for nonlinear optical processes, for example, for third-harmonic generation (THG), which would not require cooling to low temperature.

Analyzing the Kerr nonlinearity in more detail, it becomes apparent that the interaction between plasmons of different polarizations is not as trivial as assumed above: for the case of linear crosspolarized pump and probe radiation, the Kerr nonlinearity also effects the probe radiation, though the impact is only one-third of the effect for the copolarized case (see Supporting Information for derivation). The situation for the circularly polarized radiation is even more deviating from experimental observations, both probe configurations, that is, co- and counterpolarized, are expected to be identical. This is consistent with observations on conventional isotropic nonlinear materials, where no circular dichroism can be induced.^[40] However, the situation for the graphene disks goes beyond the Kerr effects for circularly polarized radiation, as the excited plasmons are related to circulating currents. The associated quasi-static

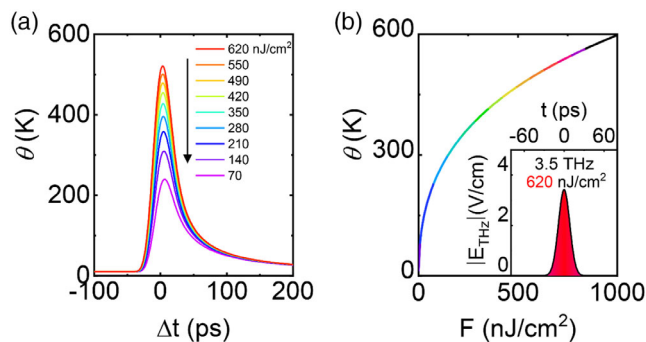


Figure 3. Electronic temperature θ . a) Calculated transient θ as a function of the delay time (Δt) for various pump fluences. b) Peak of θ as a function of the fluence. Inset shows the calculated envelope profile of the THz electric field (3.5 THz) at a fluence of 620 nJ cm^{-2} .

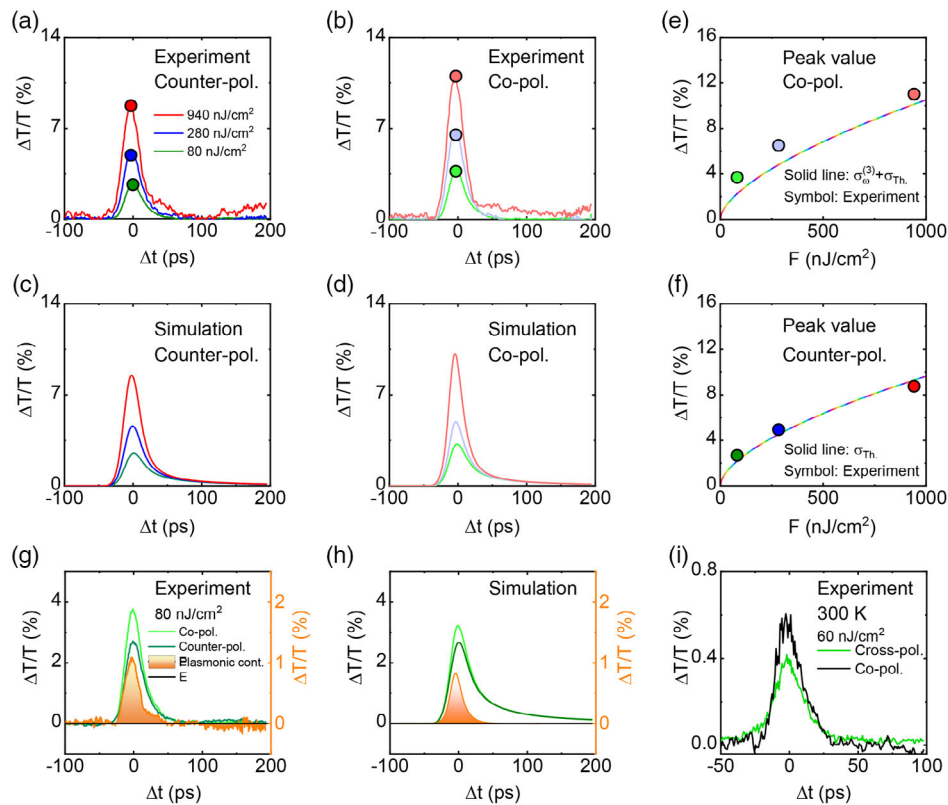


Figure 4. Change of THz transmission probed with circularly polarized radiation. Experimentally measured change of transmission $\Delta T/T$ at 3.5 THz with the a) counter- and b) copolarized pump and probe radiation. Circles mark the peak values of $\Delta T/T$. Simulated $\Delta T/T$ for c) thermal nonlinearity and d) Kerr nonlinearity. Fluence-dependent peak value of $\Delta T/T$ for e) co- and f) counterpolarized radiation. Circles shown in (e) and (f) are taken from (b) and (a), respectively; the pump fluences from (b) to (f) are identical to the one in (a). Lines denote simulation results. g) Experimentally and h) theoretically obtained plasmonic contribution (orange filling curves with right axis), retrieved by subtracting $\Delta T/T$ of copolarization from $\Delta T/T$ of counterpolarization. $\Delta T/T$ of co- and counterpolarizations are taken from (a) to (d) at the fluence of 80 nJ cm^{-2} . i) Pump-probe signals with the linearly polarized THz radiation at room temperature. Black and green curves correspond to data obtained from co- and crosspolarization configurations, respectively. Input fluence is set to 60 nJ cm^{-2} .

magnetic fields break the symmetry for left- and right-handed circularly polarized radiation,^[41] implying that co- and counterpolarized probe radiations experience different nonlinearities. An alternative picture to illustrate the actual asymmetry is the interpretation of the circular plasmon as spatial modulation of the carrier density in the disk, related to an angular momentum.^[42,43] For the copolarized case, the probe radiation experiences a static change in carrier density (and thus conductivity) for a given time delay, depending on the phase between pump and probe fields. Meanwhile, the counterpolarized radiation observes the average carrier density.

In our calculations, the third-order nonlinearity of the conductivity, $\sigma_{\omega}^{(3)}$, reduces the overall conductivity and thus quenches the absorption. In unpatterned graphene, the Kerr nonlinear susceptibility, $|\chi_{\omega}^{(3)}|$, was experimentally measured based on four-wave mixing and shown to reach the value of $1.4 \times 10^{-15} \text{ m}^2 \text{ V}^{-2}$ in the near-infrared spectral region.^[22] At such high photon energies, the optical properties are dominated by the interband process. The value of $|\chi_{\omega}^{(3)}|$ can be reached as the involved transitions are all resonant, that is, on the band

structure, regardless of the excitation and/or relaxation energy. At lower photon energies, theoretical investigations reported that third-order nonlinear susceptibility can be as high as $\approx 10^{-11} \text{ m}^2 \text{ V}^{-2}$ (at $\approx 25 \text{ THz}$) and $\approx 2.5 \times 10^{-9} \text{ m}^2 \text{ V}^{-2}$ (at $\approx 10 \text{ THz}$).^[37,44] In our study, we ascertain the Kerr nonlinear susceptibility of the graphene disks from Equation (2) as $|\chi_{\omega}^{(3)}| \approx 10^{-9} \text{ m}^2 \text{ V}^{-2}$ at ω_{p0} , which is on the order of the theoretical prediction. While the experimental setup does not allow for the measurement of THG, our model does allow us to estimate the expected efficiency. From the nonlinear conductivity, the nonlinear susceptibility $\chi_{\text{g}\omega}^{(3)}$ can be derived via $\chi_{\text{g}\omega}^{(3)} = \sigma_{3\omega}^{(3)}/ig\omega\varepsilon_0d_{\text{gr}}$ with ε_0 being the vacuum permittivity and d_{gr} being the effective thickness of bilayer graphene. g is 1 or 3 for $\chi_{\omega}^{(3)}$ or $\chi_{3\omega}^{(3)}$, respectively. From our model, we estimate the susceptibility for THG to be $|\chi_{3\omega}^{(3)}| \approx 10^{-10} \text{ m}^2 \text{ V}^{-2}$, which is about one order of magnitude smaller compared with the value ($\approx 1.7 \times 10^{-9} \text{ m}^2 \text{ V}^{-2}$) reported in unpatterned graphene.^[30] To experimentally prove the THG, a spectrally resolved measurement is required, which is beyond the scope of the current study.

3. Conclusion

In conclusion, we demonstrate clear experimental evidence of nonlinear THz absorption in graphene plasmonic elements beyond thermal effects. This plasmonic nonlinearity can be well described by the Kerr effect, that is, it is a third-order nonlinear optical process. In contrast to thermal effects, which are limited in speed by the cooling of the hot charge carriers, the lifetime of the plasmonic nonlinearity is below the temporal resolution of our experiment, which is expected as the Kerr effect is inherently linked to the driving field. Our model, which is based on hot carrier as well as Kerr effects, matches the experimental results well, further validating the robust interpretation of our study.

Supporting Information

Supporting Information is available from the Wiley Online Library or from the author.

Acknowledgements

This study was funded by the Deutsche Forschungsgemeinschaft (DFG, German Research Foundation)—Project-ID 278162697—SFB 1242. R.L.M.-W. acknowledges support by core programs at the USA Naval Research Laboratory funded by the Office of Naval Research. M.T.D. acknowledges the American Society for Engineering Education Fellowship. We thank J Michael Klopff and the ELBE team for assistance. Furthermore, we acknowledge fruitful discussion with Axel Lorke.

Correction added on 23 August 2022, after first online publication: Projekt DEAL funding statement has been added.

Open Access funding enabled and organized by Projekt DEAL.

Conflict of Interest

The authors declare no conflict of interest.

Data Availability Statement

Data available on request from the authors.

Keywords

carrier dynamics, graphene, plasmonic nonlinearities, terahertz, thermal nonlinearities

Received: July 23, 2021

Revised: October 13, 2021

Published online: December 18, 2021

- [1] L. Ju, B. Geng, J. Horng, C. Girit, M. Martin, Z. Hao, H. Bechtel, X. Liang, A. Zettl, Y. Shen, F. Wang, *Nat. Nanotechnol.* **2011**, *6*, 630.
 [2] Z. Zeng, X. Huang, Z. Yin, H. Li, Y. Chen, H. Li, Q. Zhang, J. Ma, F. Boey, H. Zhang, *Adv. Mater.* **2012**, *24*, 4138.
 [3] J. Chen, M. Badioli, P. Alonso-González, S. Thongrattanasiri, F. Huth, J. Osmond, M. Spasenović, A. Centeno, A. Pesquera, P. Godignon, A. Elorza, N. Camara, F. Abajo, R. Hillenbrand, F. Koppens, *Nature* **2012**, *487*, 77.
 [4] P. Tassin, T. Koschny, C. Soukoulis, *Science* **2013**, *341*, 620.
 [5] T. Low, P. Avouris, *ACS Nano* **2014**, *8*, 1086.

- [6] Y. Fan, N. Shen, T. Koschny, C. M. Soukoulis, *ACS Photonics* **2015**, *2*, 151.
 [7] G. Li, V. Semenenko, V. Perebeinos, P. Liu, *ACS Photonics* **2019**, *6*, 3180.
 [8] M. Jablan, H. Buljan, M. Soljačić, *Phys. Rev. B* **2009**, *80*, 245435.
 [9] X. Cai, A. Sushkov, M. Jadidi, L. Nyakiti, R. Myers-Ward, D. Kurt Gaskill, T. Murphy, M. Fuhner, H. Drew, *Nano Lett.* **2015**, *15*, 4295.
 [10] D. Bandurin, D. Svintsov, I. Gayduchenko, S. Xu, A. Principi, M. Moskotin, I. Tretyakov, D. Yagodkin, S. Zhukov, T. Taniguchi, K. Watanabe, I. Grigorieva, M. Goltsman, A. Geim, G. Fedorov, *Nat. Commun.* **2018**, *9*, 5392.
 [11] Y. Bahk, G. Ramakrishnan, J. Choi, H. Song, G. Choi, Y. Kim, K. Ahn, D. Kim, P. Planken, *ACS Nano* **2014**, *8*, 9089.
 [12] Y. Li, P. Ferreyra, A. Swan, R. Paiella, *ACS Photonics* **2019**, *6*, 2562.
 [13] L. Kim, S. Kim, P. Jha, V. Brar, H. Atwater, *Nat. Mater.* **2021**, *20*, 805.
 [14] B. Rodriguez, R. Yan, M. Zhu, D. Jena, L. Liu, H. Xing, *Appl. Phys. Lett.* **2012**, *101*, 261115.
 [15] V. Brar, M. Sherrott, M. Jang, S. Kim, L. Kim, M. Choi, L. Sweatlock, H. Atwater, *Nat. Commun.* **2015**, *6*, 7032.
 [16] D. S. Jessop, S. J. Kindness, L. Xiao, P. B. Weimer, H. Lin, Y. Ren, C. X. Ren, S. Hofmann, J. A. Zeitler, H. E. Beere, D. A. Ritchie, R. Degl'Innocenti, *Appl. Phys. Lett.* **2016**, *108*, 171101.
 [17] P. Gopalan, B. Sensale-Rodriguez, *Adv. Opt. Mater.* **2020**, *8*, 1900550.
 [18] F. Zhou, W. Du, *Appl. Opt.* **2018**, *57*, 6645.
 [19] X. Guo, R. Liu, D. Hu, H. Hu, Z. Wei, R. Wang, Y. Dai, Y. Cheng, K. Chen, K. Liu, G. Zhang, X. Zhu, Z. Sun, X. Yang, Q. Dai, *Adv. Mater.* **2020**, *32*, 1907105.
 [20] Y. Hu, J. You, M. Tong, X. Zheng, Z. Xu, X. Cheng, T. Jiang, *Adv. Sci.* **2020**, *7*, 2000799.
 [21] K. Ooi, D. Tan, *Proc. Math. Phys. Eng.* **2017**, *473*, 20170433.
 [22] E. Hendry, P. J. Hale, J. Moger, A. K. Savchenko, S. A. Mikhailov, *Phys. Rev. Lett.* **2010**, *105*, 097401.
 [23] M. Breusing, S. Kuehn, T. Winzer, E. Malić, F. Milde, N. Severin, J. P. Rabe, C. Ropers, A. Knorr, T. Elsaesser, *Phys. Rev. B* **2011**, *83*, 153410.
 [24] S. Winnerl, M. Orlita, P. Plochocka, P. Kossacki, M. Potemski, T. Winzer, E. Malic, A. Knorr, M. Sprinkle, C. Berger, W. A. de Heer, H. Schneider, M. Helm, *Phys. Rev. Lett.* **2011**, *107*, 237401.
 [25] S. Winnerl, F. Göttfert, M. Mittendorff, H. Schneider, M. Helm, T. Winzer, E. Malic, A. Knorr, M. Orlita, M. Potemski, *J. Condens. Matter Phys.* **2013**, *25*, 054202.
 [26] T. Christensen, W. Yan, A. Jauho, M. Wubs, N. Mortensen, *Phys. Rev. B* **2015**, *92*, 121407.
 [27] F. Karimi, A. H. Davoody, I. Knezevic, *Phys. Rev. B* **2018**, *97*, 245403.
 [28] H. Hafez, S. Kovalev, K. Tielrooij, M. Bonn, M. Gensch, D. Turchinovich, *Adv. Opt. Mater.* **2020**, *8*, 190077.
 [29] N. Savostianova, S. Mikhailov, *Phys. Rev. B* **2018**, *97*, 165424.
 [30] H. A. Hafez, S. Kovalev, J. C. Deinert, Z. Mics, B. Green, N. Awari, M. Chen, S. Gernanskiy, U. Lehnert, J. Teichert, Z. Wang, K. J. Tielrooij, Z. Liu, Z. Chen, A. Narita, K. Müllen, M. Bonn, M. Gensch, D. Turchinovich, *Nature* **2018**, *561*, 507.
 [31] K. M. Daniels, M. M. Jadidi, A. B. Sushkov, A. Nath, A. K. Boyd, K. Sridhara, H. D. Drew, T. E. Murphy, R. L. Myers-Ward, D. K. Gaskill, *2D Mater.* **2017**, *4*, 025034.
 [32] M. M. Jadidi, K. M. Daniels, R. L. Myers-Ward, D. K. Gaskill, J. C. König-Otto, S. Winnerl, A. B. Sushkov, H. D. Drew, T. E. Murphy, M. Mittendorff, *ACS Photonics* **2019**, *6*, 302.
 [33] M. M. Jadidi, J. C. König-Otto, S. Winnerl, A. B. Sushkov, H. D. Drew, T. E. Murphy, M. Mittendorff, *Nano Lett.* **2016**, *16*, 2734.
 [34] M. L. Chin, S. Matschy, F. Stawitzki, J. Poojali, H. Hafez, D. Turchinovich, S. Winnerl, G. Kumar, R. L. Myers-Ward, M. Dejarld, K. M. Daniels, H. D. Drew, T. E. Murphy, M. Mittendorff, *J. Phys. Photonics* **2021**, *3*, 01LT01.

- [35] A. A. Melnikov, A. A. Sokolik, A. V. Frolov, S. V. Chekalin, E. A. Ryabov, *Appl. Phys. Lett.* **2019**, *114*, 191107.
- [36] H. Yan, X. Li, B. Chandra, G. Tulevski, Y. Wu, M. Freitag, W. Zhu, P. Avouris, F. Xia, *Nat. Nanotechnol.* **2012**, *7*, 330.
- [37] J. D. Cox, I. Silveiro, F. J. G. de Abajo, *ACS Nano* **2016**, *10*, 1995.
- [38] P. Wallace, *Phys. Rev.* **1947**, *71*, 622.
- [39] A. Neto, F. Guinea, N. Peres, K. Novoselov, A. Geim, *Rev. Mod. Phys.* **2009**, *81*, 109.
- [40] I. D. Tokman, Q. Chen, I. A. Shereshevsky, V. I. Pozdnyakova, I. Qladyshkin, M. Tokman, A. Belyanin, *Phys. Rev. B* **2020**, *101*, 174429.
- [41] J. L. Oudar, *IEEE J. Quantum Electron.* **1983**, *19*, 713.
- [42] T. Müller, A. Lorke, D. Reuter, *Phys. E* **2006**, *32*, 528.
- [43] W. Lei, C. Notthoff, J. Peng, D. Reuter, A. Wieck, G. Bester, A. Lorke, *Phys. Rev. Lett.* **2010**, *105*, 176804.
- [44] J. Liu, T. Huang, P. K. Li, *Opt. Lett.* **2018**, *43*, 2102.